Arbitrary Shape Engineerable Spiral Micropseudocapacitors with Ultrahigh Energy and Power Densities

Xiaocong Tian, Mengzhu Shi, Xu Xu, Mengyu Yan, Lin Xu, Aamir Minhas-Khan, Chunhua Han, Liang He, and Liqiang Mai**

On-chip microscale energy storage devices have had a great deal of attention as micropower sources for miniaturized electronic devices due to their good size compatibility and high electrochemical performance.[1–5] As an alternative to microbatteries, microsupercapacitors (MSCs) usually deliver much higher power densities and can be fully charged and discharged in seconds.[3,6,7] Microscale interdigital electrodes, with high areal and volumetric utilization of active materials, have been considered as an effective design to achieve the high-performance MSCs.[8–13] Electrical double-layer microsupercapacitors (EDL-MSCs), the first-generation MSCs, were widely studied and fabricated in previous research.[14–19] Two main approaches, namely, minimizing the electrode thickness to atomic levels and utilizing ultrahigh-surface-area carbon materials, were employed to improve the energy densities of EDL-MSCs greatly.[16,20–27] Mullen group constructed graphene-based in-plane interdigital microsupercapacitors, which deliver an area capacitance of 80.7 μF cm^{-2} and a stack capacitance of 17.9 F cm^{-3}.[20] Meanwhile, it allows for operations at ultrahigh scan rates up to 1000 V s^{-1}.

Although a lot of inspiring works have been achieved on EDL-MSCs, the energy densities of EDL-MSCs still remain low due to their electrostatic double-layer charging based mechanism.[3,20] An effective way to further improve the areal and stack energy densities of MSCs is to develop micropseudocapacitors (MPCs) that achieve high-performance electrochemical energy storage during reversible redox reactions at low rates.[28–30] Nevertheless, due to the blocked interior electrical transport channels from active materials to current collectors, it becomes difficult to operate most reported MPCs at very fast charge–discharge rates, suggesting the low power densities.[3] Furthermore, their high energy/power densities are merely reported for ultrathin structures, which do not scale up with the thickness of the electrodes.[3,31–40] It is regarded as urgent but challenging to develop the MPCs with both ultrahigh energy and power densities up to micrometer-sized heights.

In consideration of the practical applications described above, we establish a simple and efficient strategy to achieve both ultrahigh energy and power densities of MPCs with the plantation of pillar arrays in the microspirals with ultrathin nanosheets. This efficient route provides much more interior electrical transport shortcuts and, therefore, more ions (cations and anions) in the electrolyte get access to the surface of nanosheets easily. This support also prevents active materials peeling off from the current collectors during the fabrication processes. The all-solid-state spiral-shaped three-dimensional (3D) micropseudocapacitors (SST-MPCs) with the area of ≈1.67 mm^2 and height of ≈1.7 μm deliver both ultrahigh energy density of ≈34.9 mWh cm^{-3} at the scan rate of 10 mV s^{-1} and high power density of 193.4 W cm^{-3} at the ultrahigh scan rate of 200 V s^{-1}. During the 50 000 charge and discharge cycles, the SST-MPCs also demonstrate an excellent cycling stability. More importantly, for practical applications, the novel microscale spiral-shaped design can be applied to achieve shape-engineerable MPCs and realize the unconventional series/parallel combinations which are also applicable to other pseudocapacitive materials and fields.

The fabrication processes are schematically illustrated in **Figure 1**a. E-beam lithography technique provides a direct and more precise pattern writing platform compared with lithography technique.[41] The SU-8 micropillar arrays were directly fabricated first. It can be clearly observed from Figure S1 (Supporting Information) that the fabricated micropillars are identical and arranged in two symmetrical spirals. Next, the two spiral-shaped two continuous overlays were achieved through the secondary e-beam lithography alignment (Figure S2, Supporting Information). The 3D current collectors were made through physical vapor deposition and metal sputtering techniques in the following steps (Figure S3, Supporting Information). Electrodeposition method offers an effective way to deposit active materials with high surface-area-to-volume ratio, which serve as active electrodes for electrochemical capacitors.[42] In our work, cobalt hydroxide nanosheets were first selected and fabricated as the active material. Finally, the KOH–polyvinyl alcohol (PVA) gel electrolyte was synthesized and applied to obtain the SST-MPCs.

The circular microscale energy storage unit is schematically presented in Figure 1b, where the two electrodes are stacked in microscale spiral shapes (Figure S4, Supporting Information). The basic design of the two electrodes is very similar to that of the Archimedean spiral. The spiral geometry of two micrometer-sized electrodes is equivalent but oppositely sensed

X. Tian, M. Shi, X. Xu, M. Yan, Dr. L. Xu,
Dr. A. Minhas-Khan, Dr. C. Han, Dr. L. He, Prof. L. Mai
State Key Laboratory of Advanced Technology
for Materials Synthesis and Processing
Wuhan University of Technology
Wuhan 430070, P. R. China
E-mail: hch5927@whut.edu.cn; mlq518@whut.edu.cn
X. Xu
Department of Chemistry and Biochemistry
University of California
Los Angeles, CA 90095, USA
Dr. L. Xu
Department of Chemistry and Chemical Biology
Harvard University
Cambridge, MA 02138, USA

DOI: 10.1002/adma.201503567

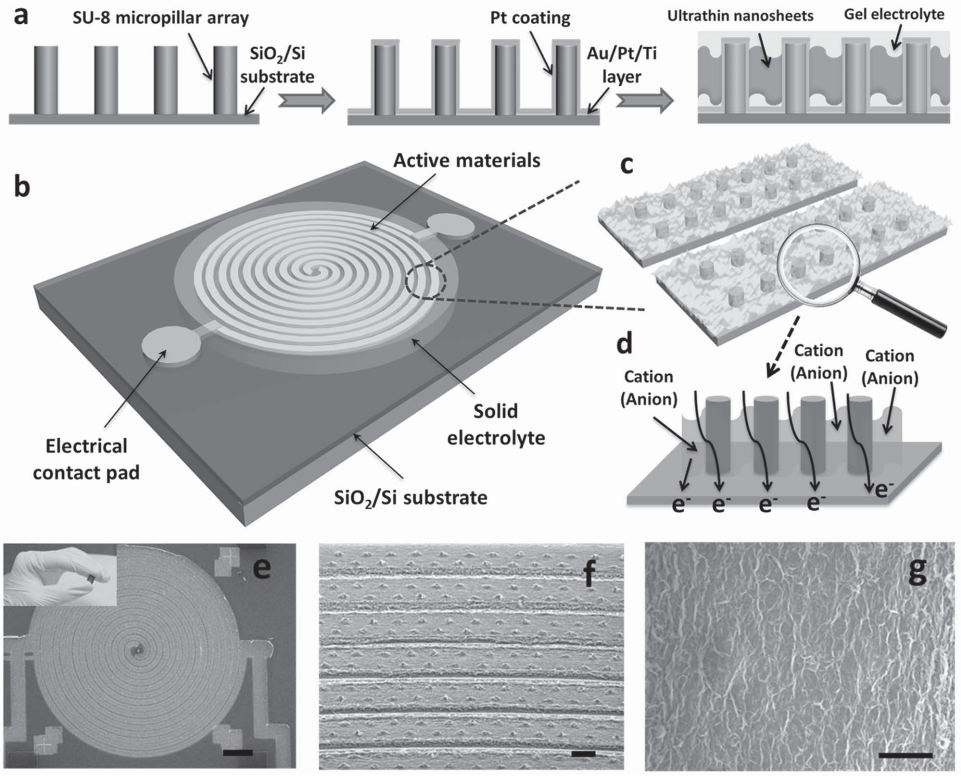

Figure 1. Fabrication and structural characterization of SST-MPCs. a) Schematic illustration of the fabrication process of SST-MPCs. b,c) Schematic illustration of SST-MPCs and selected area electrodes in SST-MPCs. d) Schematic illustration of ionic and electrical transport in SST-MPCs during the charge and discharge processes. e–g) FESEM images of SST-MPCs. The inset in (e) shows the digital camera image of on-chip SST-MPCs. Scale bar: e) 200, f) 10, and g) 5 μm.

in which one spiral situated closely to the another spiral in the same plane. This kind of design gradually represents as a rayed architecture.[43] In our design, the regular width of each current collector and the interspace between neighboring current collector are 30 and 15 μm, respectively. This design enables an ultrahigh area and volume utilization ratio of electrodes. Notably, during the electrochemical deposition process, the width of each microelectrode is larger than that of current collector due to the fact that the growth of deposited active materials expands on the edges of the current collector, which further improves the area and volume utilization ratio of electrodes. As is shown in Figure 1c, the highly conductive platinum-coated SU-8 micropillar arrays constitute the 3D current collector, on which the growth of the active materials occurs. The pillared 3D current collectors can provide more interior electrical transport shortcuts as shown in Figure 1d. In this experiment, the typical active materials were electrochemically deposited on the micropillar arrays. The crystal structures of active materials are demonstrated in the X-ray diffraction (XRD) pattern (Figure S5, Supporting Information), where all the diffraction peaks are indexed to the hexagonal cobalt hydroxide phase (JCPDS Card Nos. 02-0925 and 89-8616). No peaks of any other phases are detected, indicating the high purity of the cobalt hydroxide nanomaterials. It is clearly confirmed from field emission scanning electron microscopic (FESEM) images (Figure 1e–g) and transmission electron microscopic (TEM) image (Figure S6, Supporting Information) that as-deposited active materials present the ultrathin nanosheet morphology. For fair comparison, the spiral-shaped MPCs without micropillar arrays (SS-MPCs) were also carried out on the same shape current collectors (Figure S7, Supporting Information).

To evaluate the energy and power capability of SST-MPCs, cyclic voltammetry (CV) measurements were first performed at various scan rates ranging from 0.01 to 200 V s^{-1} (**Figure 2**a–c). At the low scan rate of 10 mV s^{-1}, the CV curve indicates that there may exist the Faradaic reactions during the charge and discharge processes, which indicates the high pseudocapacitance for the SST-MPCs. The high stack and areal capacitance is mainly attributed to the reversible formation of Co^{2+}/Co^{3+} redox couple in the alkali electrolytes, where the oxidation process occurs during the extraction of protons from cobalt hydroxide nanosheets according to the following equation

$$Co(OH)_2 + OH^- \leftrightarrow CoOOH + H_2O + e^- \quad (1)$$

To understand the intrinsic properties of the MSCs, the stack capacitance, energy and power densities are calculated and evaluated.[3,28–37,44] The stack and areal capacitances of SST-MPCs are calculated at various scan rates on the basis of CV curve lines. At the low scan rate of 10 mV s^{-1}, the SST-MPCs show an ultrahigh stack capacitance of 393.7 F cm^{-3} and energy density of 34.9 mWh cm^{-3} (Figure 2d). When normalized to the total mass of active materials, the specific capacitance and energy density of SST-MPCs are up to 278.7 F g^{-1} and 24.7 Wh kg^{-1},

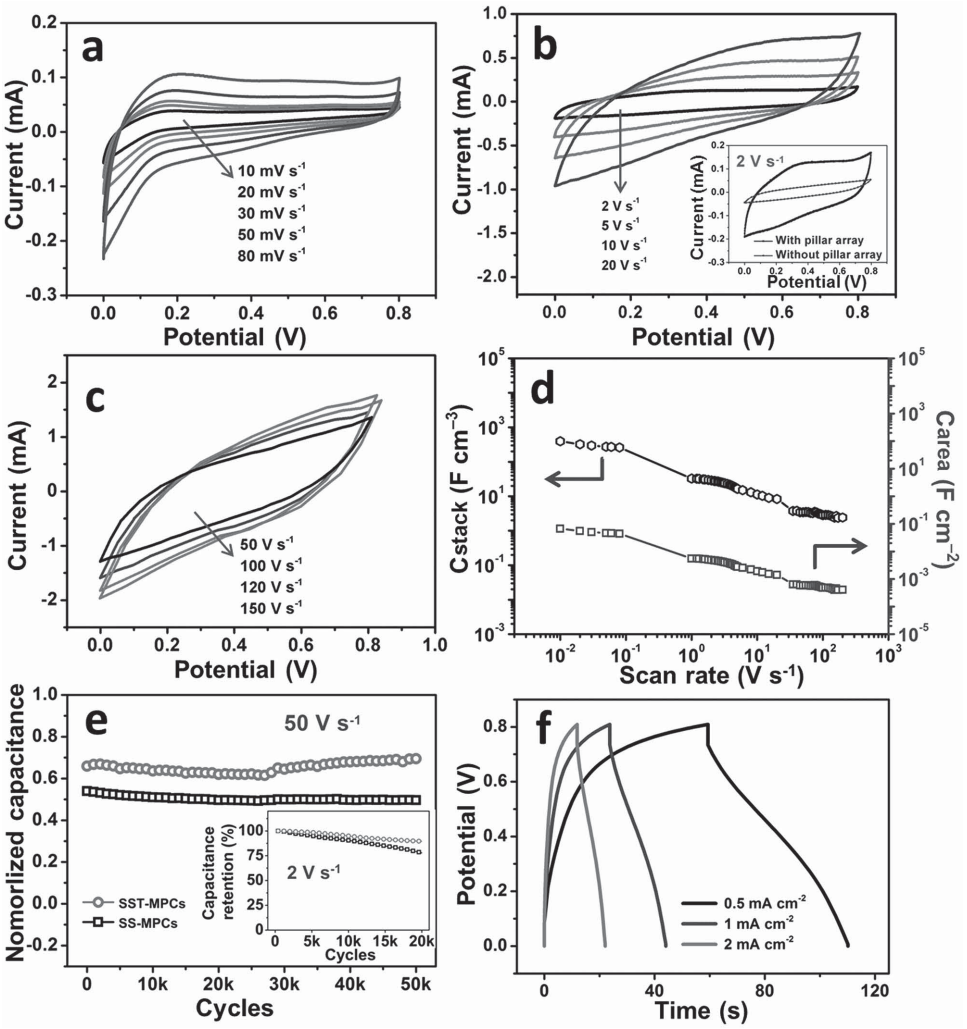

Figure 2. Electrochemical characterizations of SST-MPCs. a–c) CV curves obtained at different scan rates. The inset in (b) represents the CV curves for the devices with/without the pillar array at the scan rate of 2 V s^{-1}. d) Evolution of the stack/areal capacitance at different scan rates of SST-MPCs. e) Cycling stability (normalized) of the as-prepared SST-MPCs and SS-MPCs at the scan rate of 50 V s^{-1} over 50 000 cycles, where SST-MPCs show the excellent stability and much higher capacitance compared with SS-MPCs. The inset in (e) represents the capacitance retention of SS-MPCs and SST-MPCs at the scan rate of 2 V s^{-1} for 20 000 charge–discharge cycles. f) Galvanostatic charge/discharge curve of SST-MPCs at various current densities.

respectively, at the scan rate of 10 mV s^{-1}. The bare platinum electrode-based MPCs were also fabricated and their electrochemical behavior was evaluated. The current of bare platinum electrodes based MPCs is much lower compared with that of SST-MPCs (Figure S8, Supporting Information), which implies that the capacitance of SST-MPCs is mainly contributed from active materials. The capacitance of SST-MPCs yields a greatly increased capacitance by four times compared with that of SS-MPCs at the scan rate of 2 V s^{-1} (inset of Figure 2b). At a very high scan rate of 200 V s^{-1}, it shows a very high power density delivering of 193.4 W cm^{-3}. It is worth noting that the high energy density of SST-MPCs is achieved at low power density and vice versa, which are consistent with previous work (Figure S9, Supporting Information).[35–37] Although the Faradaic reactions gradually decrease at increasing scan rates, it is believed that these redox activities still contribute to the high pseudocapacitance. The cycling behaviors of SS-MPCs and SST-MPCs are evaluated as shown in Figure 2e. At the scan rate of 2 V s^{-1}, the SST-MPCs hold 89.6% capacitance retention after 20 000 charge–discharge cycles, which is higher than that of SS-MPCs (77.9%). At the much higher scan rate of 50 V s^{-1}, SST-MPCs still exhibit an exceptionally enhanced electrochemical performance with the stack capacitance of 4.6 F cm^{-3}, which shows the 24% improvements compared with SS-MPCs. After 50 000 charge and discharge cycles, the capacitance of SST-MPCs maintained at 4.8 F cm^{-3}, which shows an excellent cycling stability. At ultrahigh scan rates, the high surface area becomes largest part for high power delivering.

The galvanostatic charge–discharge measurements and electrochemical impedance spectroscopy analysis were carried out to further investigate the electrochemical behaviors of micropseudocapacitors. The capacitance of SST-MPCs is up to 201.2 F cm^{-3} at the current density of 0.5 mA cm^{-2}, while the Coulombic efficiency is ≈85.6% (Figure 2f). When the current density increases greatly to 12.5 mA cm^{-2}, the Coulombic efficiency is improved to 92.9%. The specific capacitance of

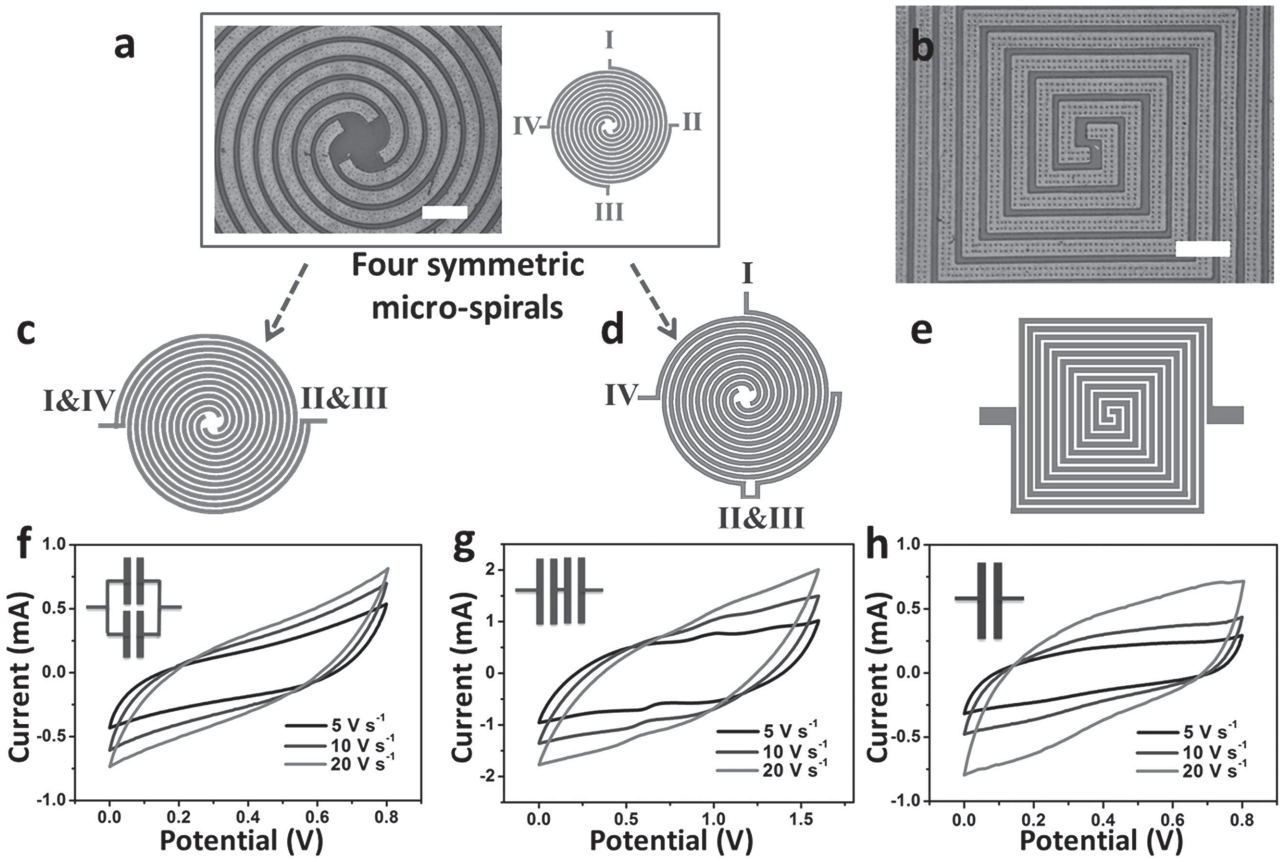

Figure 3. Series/parallel combination using spiral-shaped design and shape-engineerable MPCs. a) Optical image and schematic illustration of four symmetric electrodes based MPCs. b) Optical image of rectangular symmetrical MPCs. c,d) Schematic and equivalent circuits with parallel/series combination using four-electrodes based MPCs. e) Schematic illustration of rectangular symmetrical MPCs. CV curves obtained at different scan rates for f) parallel and g) series combined MPCs, respectively. h) CV curves of rectangular MPCs obtained at different scan rates. Scale bar: a,b) 100 μm.

SST-MPCs is demonstrated much higher than that of SS-MPCs (Figure S10, Supporting Information) and the improvement in electrochemical behaviors may attribute to the more interior electrical transport shortcuts in the microscale electrodes. In addition, the incremental voltage drop of SS-MPCs compared with SST-MPCs indicates the important role of pillar arrays in the microspirals with ultrathin nanosheets. The smaller equivalent series resistance (ESR) values as shown in a Nyquist plot (Figure S11, Supporting Information) also confirm the improvement in electrical transport of SST-MPCs compared with SS-MPCs. It is widely acknowledged that the maximum power density (P_{max}) is a fundamental property for supercapacitors. Based on the ESR value, the maximum power density of SST-MPCs is calculated by $P_{max} = V_i^2/(4 \times ESR \times V)$ where V_i represents initial voltage and V is donated as the total volume of the device.[45] The maximum power density of SST-MPCs is close to 850 W cm^{-3}, approaching the power density of electrolytic capacitors. Moreover, the excellent power response with very short RC time constant (τ_0 = 4.9 ms) for SST-MPCs is much superior to that of SS-MPCs. To the best of our knowledge, the MPCs with such excellent performance in terms of both ultrahigh energy and power densities were rarely reported.

Another type of active materials, Na^+-intercalated manganese dioxide (NMD) nanomaterials, was also employed to further identify the applicability of this design. A constant current is applied in the three-electrode system during the electrodeposition processes to grow on the current collectors.[46] The morphology of NMD nanomaterials has been characterized by FESEM measurements, which show the nanoflower structures (Figure S12, Supporting Information). Then, the electrochemical performance of NMD nanoflowers-based MPCs was also tested in the two-electrode system (Figure S13, Supporting Information). The reversible redox reactions of NMD-based MPCs can be described as follows

$$Na_xMnO_2 + H_2O + e^- \leftrightarrow Na_xMnOOH + OH^- \quad (2)$$

At the scan rate of 10 mV s^{-1}, the specific capacitance of NMD-based MPCs is up to 118.5 F cm^{-3} which further demonstrated the excellent electrochemical behaviors in our design.

Previous research attempts to connect MSCs in series/parallel combination to get integrated energy storage devices with higher potential/current.[3] Different from interdigital microscale electrodes, the spiral-shaped microscale electrodes enable the series/parallel combination in a very unique way. As it is shown in **Figure 3**a, there are four spiral-shaped symmetrical microscale electrodes whose regular width still remains at ≈15 μm. By adjusting the connection ways of these four

microscale electrodes, the parallel/series combination can be both realized in the same configuration (Figure 3c,d). To obtain the series combination, two neighboring microscale electrodes (II and III electrodes) are connected, and the other two neighboring microscale electrodes (I and IV electrodes) are taken as measured electrodes (Figure 3c). In another way, connecting the each two neighboring microscale electrodes as two counter electrodes can achieve the parallel combination (Figure 3d). It is clearly demonstrated that the spiral-shaped design provides great controllability and potential in series/parallel combination. Notably, according to the electrochemical measurement results (Figure 3f,g), it is found that the series combination would greatly increase the power densities of the MPCs, and the parallel combination may be more suitable for very high scan rate compared with the individual MPC. Therefore, the spiral-shaped MPCs have the great potential for delivering high power and energy densities.

To realize the maximum areal and stack capacitance, the microscale electrode designs play a great role in the utilization ratio of active materials per unit area. Interdigital electrode design can provide ultrahigh utilization ratio of active materials per unit area, which may therefore result in the high area and stack capacitance.[3] However, interdigital electrodes could not meet the requirements to fabricate the microscale energy storage devices with controllable geometry. Here, we utilize the novel spiral-shaped design to realize the ultrahigh utilization ratio of active materials per unit area and controllable geometry. According to the principle concept of the Archimedean spiral, this design represents the rayed shapes which start from the center of the spirals. By adjusting the spiral shape without changing the width of each current collector and the interspace between neighboring current collector, the rectangular MPCs are engineered (Figure 3b,e), where the high electrochemical performance can also be realized (Figure 3h). It is believed that the electric field distribution between the microscale electrodes differs in different shapes and the changes in ions transport path could result in some unexpected changes in electrochemical performance.[47] This spiral-shaped design can ensure the MPCs to be emerged as arbitrary microshapes, which could realize the maximum usage of any microregions.

The Ragone plots in regard to the stack and areal capacitance calculated through CV data are both provided in **Figure 4** which clearly demonstrates the great advantages of SST-MPCs. It can be seen from Figure 4a that the specific stack energy density of SST-MPCs (at the scan rate of 10 mV s^{-1}) is approximately two orders higher than that of reported MSCs with graphene/carbon nanotube carpets (G/CNTCs),[48] RGO/MnO_2/AgNW (RGMA) in aqueous electrolyte,[33] and laser-scribed graphene/single-wall (LSG-SWSNTs).[49] Compared with reported RGMA in ionic liquids (ILs) and MnO_x/Au multilayers based MSCs,[28] the stack energy density of SST-MPCs (at the scan rate of 10 mV s^{-1}) is more than one order higher. Notably, the power density achieved in our work measured at very high scan rates also advances reported MSCs. In addition, another key performance metrics of MSCs are the areal energy and power densities due to their small footprint area of the devices and these values are strongly influenced by electrode architectures, especially the thicknesses of MSCs. In consideration of the fact that the thickness of G/CNTCs based MSCs is up to 20 μm, the areal energy density of G/CNTCs based MSCs is still one order lower than SST-MPCs, which further demonstrates the great potential of SST-MPCs for on-chip applications (Figure 4b). Although the energy density of SST-MPCs becomes lower than G/CNTCs based MSCs at ultrahigh scan rates, the areal power density of SST-MPCs reaches at the same level compared with the much thicker G/CNTCs based MSCs. Thus, the great advantages of in-plane architecture of SST-MPCs outweigh the disadvantage. Moreover, based on the real galvanostatic charge–discharge method, this comparison between SST-MPCs and reported MSCs with thicker LSG (7.6 μm) was also made as shown in Figure S14 (Supporting Information). Compared with reported MSCs with LSG, SST-MPCs can deliver much higher volumetric and areal energy density with comparable volumetric power density. The Ragone plots clearly confirm the desirable electrochemical performance of SST-MPCs in both stack and areal energy and power densities.

The ultrahigh energy and power densities of SST-MPCs are mainly attributed to the high pseudocapacitive properties of active materials and narrow interelectrode gaps fabricated by e-beam lithography. Cobalt hydroxide and manganese dioxide ultrathin nanosheets are both regarded as typical pseudocapacitive materials for interfacial Faradaic reactions. The e-beam lithography technique enables narrow interelectrode gaps and results in the more active materials loading in a limited space. Thus, much more nanosheet surface is exposed to electrolyte for high stack capacitance. Combining with pillared 3D current

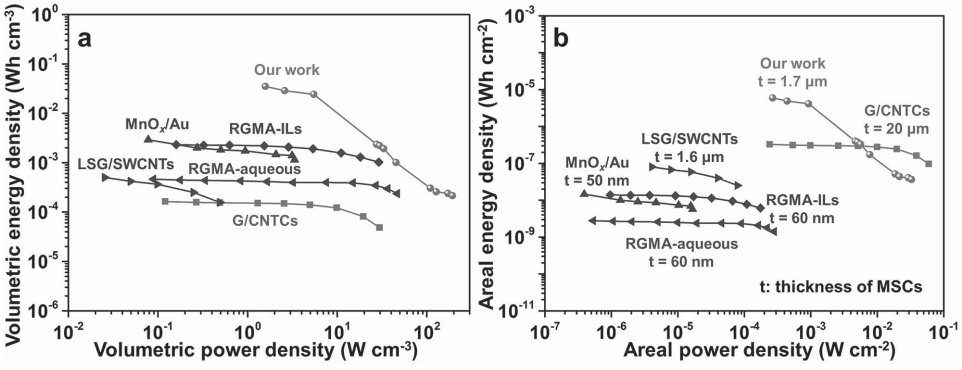

Figure 4. Comparison, in Ragone plots, of a) volumetric and b) areal specific energy and power densities of SST-MPCs with reported MSCs with MnO_x/Au multilayers, RGMA ternary hybrid film using ILs and aqueous electrolyte, G/CNTCs and LSG-SWSNTs.

collectors, the ionic transport between the microscale electrodes can also be improved during the charge and discharge processes. Moreover, from the perspective of micromechanics, this support could enable the nanosheets to be anchored between pillar arrays, preventing them from peeling off from the current collectors during the fabrication processes. The interdigital micropseudocapacitors were further fabricated using the same method. The area and volume of fabricated interdigital MPCs are almost same with that of SST-MPCs. However, with the wider interelectrode gaps (Figure S15, Supporting Information), the charge–discharge current of interdigital MPCs is lower compared with that of SST-MPCs, which demonstrates that the electrochemical behavior is very relevant to the interelectrode gap. The simulation of the electrical field distributions of circular and rectangular spiral-shaped MPCs was further carried out and analyzed as shown in Figure S16 (Supporting Information). It is observed that the uniformly distributed electrical field exists between circular interdigitated electrodes in the Archimedean spiral-shaped design due to the constant interspace between them. For rectangular SST-MPCs, the electrical field distribution is almost same with circular SST-MPCs except at the corners of rectangular. The calculated electrical field distributions further demonstrate the desirable ions transport directions in the electrolyte during the charge and discharge processes.

In summary, all-solid-state 3D on-chip MPCs with ultrahigh energy and power densities are fabricated. The excellent electrochemical performance can be attributed to the high pseudocapacitive properties of active materials and narrow interelectrode gaps fabricated by e-beam lithography. During the charge and discharge processes, the SST-MPCs exhibit excellent cycling stability. More importantly, this spiral-shaped design can ensure the MPCs to be engineerably emerged in any shapes. Furthermore, the unconventional series/parallel combinations are easily realized in spiral-shaped design, which can meet the energy and power needs in various practical applications such as microelectromechanical systems, microrobots, and implantable medical devices. Our spiral-shaped designs are expected to act as the efficient energy storage design for electronic devices, which is regarded as a general architecture for micro-/nanoscale power sources.

Experimental Section

First, the SU-8 2002 (MicroChem) was spin-coated twice on the SiO_2 / Si substrate at 3000 rpm for 30 s and annealed at 65 and 95 °C for 5 min to achieve the cure of the polymer and then the spiral-shaped SU-8 micropillar array was directly fabricated by e-beam lithography technique and develop treatment; second, methyl methacrylate (MMA, MicroChem) and poly(methyl methacrylate) (PMMA, MicroChem) were spin-coated at 4000 rpm for 30 s and annealed at 180 °C for 5 min to achieve the cure of the polymer. Then, e-beam lithography alignment was conducted and the develop process was carried out to obtain two spiral-shaped two continuous overlays; third, 5 nm Ti layer was deposited by physical vapor deposition and ≈50 nm Pt coating on the SU-8 micropillar array was achieved through the metal sputtering technique. The 50 nm Au layer was then deposited on wafer by physical vapor deposition and the MMA/PMMA was removed through the lift-off process; fourth, the ultrathin cobalt hydroxide and manganese dioxides nanosheets were electrodeposited on the 3D current collectors by Autolab PGSTAT 302N at the constant potential of −1 V in 0.025 M $Co(NO_3)_2{\cdot}6H_2O$ solution[50] and at the constant current of 10 μA in 0.25×10^{-3} M $Mn(CH_3COO)_2$ mixed with 0.1 M CH_3COONa, respectively, in three-electrode system where Hg/HgO used as the reference electrode, Pt foil acted as the counterelectrode, and microelectrodes were the working electrode; and finally, the KOH–PVA gel electrolyte was spin-coated on the MPCs and then removed the whole water to obtain SST-MPCs. The KOH–PVA gel electrolyte was prepared as follows: 1 g of KOH was added into 10 mL of deionized water, and then 1 g of PVA powder was added. The whole mixture was heated to 90 °C under stirring until the solution became clear.

Supporting Information

Supporting Information is available from the Wiley Online Library or from the author.

Acknowledgements

X.T. and M.S. contributed equally to this work. This work was supported by the National Basic Research Program of China (2013CB934103, 2012CB933003), the International Science and Technology Cooperation Program of China (2013DFA50840), the National Natural Science Foundation of China (51302203, 51272197), the National Science Fund for Distinguished Young Scholars (51425204), the Hubei Science Fund for Distinguished Young Scholars (2014CFA035), and the Fundamental Research Funds for the Central Universities (WUT: 2015--021, 2015-CL-A1-03). The authors are deeply thankful to Prof. Charles M. Lieber of Harvard University, Prof. Dongyuan Zhao of Fudan University, and Prof. Jun Liu of Pacific Northwest National Laboratory for their stimulating discussion and kind help.

Received: July 22, 2015
Revised: August 23, 2015
Published online: October 13, 2015

[1] J. Chmiola, C. Largeot, P.-L. Taberna, P. Simon, Y. Gogotsi, *Science* **2010**, *328*, 480.
[2] L. Mai, X. Tian, X. Xu, L. Chang, L. Xu, *Chem. Rev.* **2014**, *114*, 11828.
[3] M. Beidaghi, Y. Gogotsi, *Energy Environ. Sci.* **2014**, *7*, 867.
[4] M. F. El-Kady, R. B. Kaner, *Nat. Commun.* **2013**, *4*, 1475.
[5] D. Pech, M. Brunet, H. Durou, P. Huang, V. Mochalin, Y. Gogotsi, P.-L. Taberna, P. Simon, *Nat. Nanotechnol.* **2010**, *5*, 651.
[6] M. Winter, R. J. Brodd, *Chem. Rev.* **2004**, *104*, 4245.
[7] A. D. Pasquier, I. Plitz, S. Menocal, G. Amatucci, *J. Power Sources* **2003**, *115*, 171.
[8] S. Y. Hong, J. Yoon, S. W. Jin, Y. Lim, S.-J. Lee, G. Zi, J. S. Ha, *ACS Nano* **2014**, *8*, 8844.
[9] T. M. Dinh, K. Armstrong, D. Guay, D. Pech, *J. Mater. Chem. A* **2014**, *2*, 7170.
[10] J. W. Long, B. Dunn, D. R. Rolison, H. S. White, *Chem. Rev.* **2004**, *104*, 4463.
[11] D. Pech, M. Brunet, T. M. Dinh, K. Armstrong, J. Gaudet, D. Guay, *J. Power Sources* **2013**, *230*, 230.
[12] C. Shen, X. Wang, W. Zhang, F. Kang, *J. Power Sources* **2011**, *196*, 10465.
[13] Y. Zhu, S. Murali, M. D. Stoller, K. J. Ganesh, W. Cai, P. J. Ferreira, A. Pirkle, R. M. Wallace, K. A. Cychosz, M. Thommes, D. Su, E. A. Stach, R. S. Ruoff, *Science* **2011**, *332*, 1537.
[14] S. K. Kim, H. J. Koo, A. Lee, P. V. Braun, *Adv. Mater.* **2014**, *26*, 5108.
[15] D. Kim, G. Shin, Y. J. Kang, W. Kim, J. S. Ha, *ACS Nano* **2013**, *7*, 7975.
[16] M. S. Kim, B. Hsia, C. Carraro, R. Maboudian, *Carbon* **2014**, *74*, 163.
[17] S. Liu, J. Xie, H. Li, Y. Wang, H. Y. Yang, T. Zhu, S. Zhang, G. Cao, X. Zhao, *J. Mater. Chem. A* **2014**, *2*, 18125.

[18] J. Chang, S. Adhikari, T. H. Lee, B. Li, F. Yao, D. T. Pham, V. T. Le, Y. H. Lee, *Adv. Energy Mater.* **2015**, *5*, 1500003.
[19] S. Li, X. Wang, *J. Power Sources* **2015**, *282*, 394.
[20] Z. S. Wu, K. Parvez, X. Feng, K. Müllen, *Nat. Commun.* **2013**, *4*, 2487.
[21] Z.-S. Wu, K. Parvez, A. Winter, H. Vieker, X. Liu, S. Han, A. Turchanin, X. Feng, K. Müllen, *Adv. Mater.* **2014**, *26*, 4552.
[22] Z. S. Wu, K. Parvez, X. Feng, K. Müllen, *J. Mater. Chem. A* **2014**, *2*, 8288.
[23] Z. Niu, L. Zhang, L. Liu, B. Zhu, H. Dong, X. Chen, *Adv. Mater.* **2013**, *25*, 4035.
[24] M. F. El-Kady, V. Strong, S. Dubin, R. B. Kaner, *Science* **2012**, *335*, 1326.
[25] W. Gao, N. Singh, L. Song, Z. Liu, A. L. M. Reddy, L. Ci, R. Vajtai, Q. Zhang, B. Wei, P. M. Ajayan, *Nat. Nanotechnol.* **2011**, *6*, 496.
[26] J. Ren, L. Li, C. Chen, X. Chen, Z. Cai, L. Qiu, Y. Wang, X. Zhu, H. Peng, *Adv. Mater.* **2013**, *25*, 1155.
[27] W. W. Liu, Y. Q. Feng, X. B. Yan, J. T. Chen, Q. J. Xue, *Adv. Funct. Mater.* **2013**, *23*, 4111.
[28] W. Si, C. Yan, Y. Chen, S. Oswald, L. Han, O. G. Schmidt, *Energy Environ. Sci.* **2013**, *6*, 3218.
[29] J. Han, Y.-C. Lin, L. Chen, Y.-C. Tsai, Y. Ito, X. Guo, A. Hirata, T. Fujita, M. Esashi, T. Gessner, M. Chen, *Adv. Sci.* **2015**, *2*, 1500067.
[30] K. Wang, W. Zou, B. Quan, A. Yu, H. Wu, P. Jiang, Z. Wei, *Adv. Energy Mater.* **2011**, *1*, 1068.
[31] L. Cao, S. Yang, W. Gao, Z. Liu, Y. Gong, L. Ma, G. Shi, S. Lei, Y. Zhang, S. Zhang, R. Vajtai, P. M. Ajayan, *Small* **2013**, *9*, 2905.
[32] W. Liu, X. Yan, J. Chen, Y. Feng, Q. Xue, *Nanoscale* **2013**, *5*, 6053.
[33] W. Liu, C. Lu, X. Wang, R. Y. Tay, B. K. Tay, *ACS Nano* **2015**, *9*, 1528.
[34] J. Feng, X. Sun, C. Wu, L. Peng, C. Lin, S. Hu, J. Yang, Y. Xie, *J. Am. Chem. Soc.* **2011**, *133*, 17832.
[35] X. Wang, Y. Yin, X. Li, Z. You, *J. Power Sources* **2014**, *252*, 64.
[36] C. Meng, J. Maeng, S. W. M. John, P. P. Irazoqui, *Adv. Energy Mater.* **2014**, *4*, 1301269.
[37] L. Peng, X. Peng, B. Liu, C. Wu, Y. Xie, G. Yu, *Nano Lett.* **2013**, *13*, 2151.
[38] P. Simon, Y. Gogotsi, B. Dunn, *Science* **2014**, *343*, 1210.
[39] Y. Gogotsi, P. Simon, *Science* **2011**, *334*, 917.
[40] P. Simon, Y. Gogotsi, *Acc. Chem. Res.* **2013**, *46*, 1094.
[41] V. R. Manfrinato, L. Zhang, D. Su, H. Duan, R. G. Hobbs, E. A. Stach, K. K. Berggren, *Nano Lett.* **2013**, *13*, 1555.
[42] J. Duay, S. A. Sherrill, Z. Gui, E. Gillette, S. B. Lee, *ACS Nano* **2013**, *7*, 1200.
[43] J. A. Kaiser, *IEEE Trans. Antennas Propag.* **1960**, *8*, 312.
[44] S. Zhang, N. Pan, *Adv. Energy Mater.* **2015**, *5*, 1401401.
[45] Z. Fan, J. Yan, T. Wei, L. Zhi, G. Ning, T. Li, F. Wei, *Adv. Funct. Mater.* **2011**, *21*, 2366.
[46] L. Mai, H. Li, Y. Zhao, L. Xu, X. Xu, Y. Luo, Z. Zhang, W. Ke, C. Niu, Q. Zhang, *Sci. Rep.* **2013**, *3*, 1718.
[47] R. W. Hart, H. S. White, B. Dunn, D. R. Rolison, *Electrochem. Commun.* **2003**, *5*, 120.
[48] J. Lin, C. Zhang, Z. Yan, Y. Zhu, Z. Peng, R. H. Hauge, D. Natelson, J. M. Tour, *Nano Lett.* **2013**, *13*, 72.
[49] F. Wen, C. Hao, J. Xiang, L. Wang, H. Hou, Z. Su, W. Hu, Z. Liu, *Carbon* **2014**, *75*, 236.
[50] C. Yuan, L. Yang, L. Hou, L. Shen, X. Zhang, X. W. D. Lou, *Energy Environ. Sci.* **2012**, *5*, 7883.